Inorganic Chemistry

Article

pubs.acs.org/IC

Theoretical and Experimental Insight on Ag_2CrO_4 Microcrystals: Synthesis, Characterization, and Photoluminescence Properties

Gabriela S. Silva,[†] Lourdes Gracia,*[,‡] Maria T. Fabbro,[†] Luis P. Serejo dos Santos,[†] Hector Beltrán-Mir,[§] Eloisa Cordoncillo,[§] Elson Longo,[†] and Juan Andrés[‡]

[†]CDMF-UFSCar-Universidade Federal de São Carlos, P.O. Box 676, CEP, 13565-905 São Carlos, São Paulo, Brazil

[‡]Department of Analytical and Physical Chemistry and [§]Department of Inorganic and Organic Chemistry, University Jaume I (UJI), Castelló 12071, Spain

Supporting Information

ABSTRACT: Ag_2CrO_4 microcrystals were synthesized by means of the coprecipitation method without the use of a surfactant under three different conditions. On the basis of the theoretical and experimental results, we describe the relationship among the structural order/disorder effects, morphology, and photoluminescence of the Ag_2CrO_4 microcrystals. The experimental results were correlated with the theoretical findings for a deeper understanding of the relationship between the electronic structure, morphology, and photoluminescence properties. First-principles computational studies were used to calculate the geometries of bulk Ag_2CrO_4 and its low-index (001), (011), (110), (010), (111), and (100) facets based on a slab model. A good agreement between the experimental and the theoretical morphologies was found by varying the ratio of the superficial energy values.

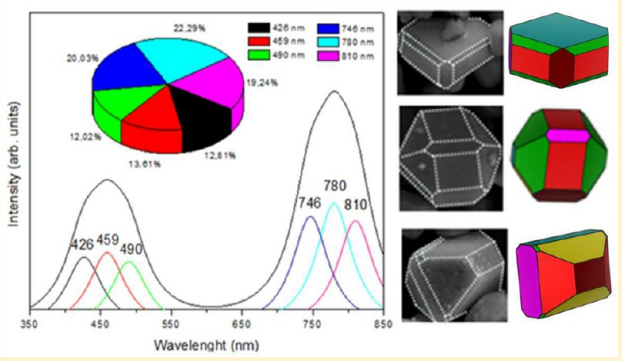

1. INTRODUCTION

Silver chromate, Ag_2CrO_4, belongs to the important chromate family of Ag-containing compounds with the formula Ag_2MO_4 (M = Cr, Mo, W).[1] Ag_2CrO_4-based materials have been the subject of extensive research because of their excellent applications in different branches of science and technology such as cathodes for lithium cells and catalysts.[1−8] In recent years, different synthetic methods have been used to obtain Ag_2CrO_4 such as coprecipitation,[9,10] hydrothermal,[11] microwave hydrothermal,[2] reversed micellar,[12] sonochemical,[6] microemulsion,[8] and template methods.[13] In addition, several chromites have been prepared using a simple coprecipitation method.[14,15] Very recently, we carried out a combined experimental and theoretical study to understand the formation and growth of Ag nanoparticles of Ag_2CrO_4 induced by electron irradiation using an electron microscope.[9]

It is well known that the controlled synthesis of specific morphologies of a given material is fundamental to obtain the required physical and chemical properties and enhance the performance in practical applications of micro- and nanomaterials.[16,17] In particular, we propose the combined use of experimental findings and first-principles calculations to reach a deeper knowledge of the electronic, structural, and energetic properties controlling the morphology, as previously reported by our research group.[18−24] In the field of material research, molybdenum- and tungsten-based oxides constitute an important class of compounds that exhibits an interesting combination of structural, chemical, and spectroscopic properties with various functional applications in different branches of science and technology.[1,25−36] Within this general framework, we are engaged in a research project that is concerned with the synthesis, characterization, and technological applications of a family of Ag-based complex metal oxides, such as α-Ag_2WO_4,[21,37] β-Ag_2WO_4,[38] β-Ag_2MoO_4,[23] and β-$AgVO_3$,[39] or Ag-containing salts such as Ag_3PO_4.[22] In particular, a relationship between the morphology and the properties such as facet-dependent photocatalytic and antibacterial properties in α-Ag_2WO_4 crystals is found.[21] We rationalized the morphological, structural, and optical properties of β-Ag_2MoO_4 microcrystals[23] and found a relationship between the photoluminescence and the photocatalytic properties of Ag_3PO_4 microcrystals.[22] In these papers, one can find our method and it presupposes the ability to calculate the surface energies, whose values enter into the Wulff construction to obtain the morphology.

In this work, we present the experimental and theoretical studies devoted to analyze the effects of different preparation conditions on the electronic structure, morphology, and photoluminescence properties of Ag_2CrO_4. First, we synthesized Ag_2CrO_4 samples by varying parameters such as the velocity of addition and presence/absence of ultrasonic irradiation using the coprecipitation method. Structural, morphological, and optical characterization was carried out

Received: June 15, 2016
Published: August 11, 2016

DOI: 10.1021/acs.inorgchem.6b01452
Inorg. Chem. 2016, 55, 8961−8970

using experimental techniques such as X-ray diffraction (XRD) with Rietveld analysis, micro-Raman (MR) spectroscopy, field-emission scanning electron microscopy (FE-SEM), ultraviolet−visible (UV−vis) diffuse reflectance spectroscopy, and photoluminescence (PL). Subsequently, we observed the effects of the different preparation conditions on the structural order/disorder effects at long and short range and on the morphology.

The paper is organized as follows: the experimental procedure is presented in section 2, the theoretical procedure is presented in section 3, and section 4 is focused on the discussion of the results on the structural, morphological, and optical properties. Finally, the conclusions are presented in section 5.

2. SYNTHESIS AND CHARACTERIZATION

Ag_2CrO_4 microcrystals were synthesized by the coprecipitation method without the use of any surfactant under three different conditions. First, 50 mL of distilled water was added to 1×10^{-3} mol of $Na_2CrO_4 \cdot 2H_2O$ (99.5% pure, Alfa Aesar). This solution remained under magnetic stirring until it turned completely homogeneous, transparent, and yellowish. Parallel to this process, 2×10^{-3} mol of $AgNO_3$ (99.8% pure, Alfa Aesar) was dissolved in 50 mL of distilled water. When both solutions turned homogeneous, the temperatures of both solutions were increased to approximately 90 °C. The addition of the Ag salt solution to the chromate salt solution was carried out dropwise by rapid injection in the presence or absence of sonication. In sample 1, the addition rate of $AgNO_3$ into Na_2CrO_4 was 25 mL/s, whereas, in samples 2 and 3 the addition rate was 10 mL/min. The difference between samples 2 and 3 was that the latter was sonicated for 10 min. For ultrasound irradiation of sample 3, the sonicator was introduced into the chromate salt solution and the irradiation was performed along with the addition process (see Figure 1). At all

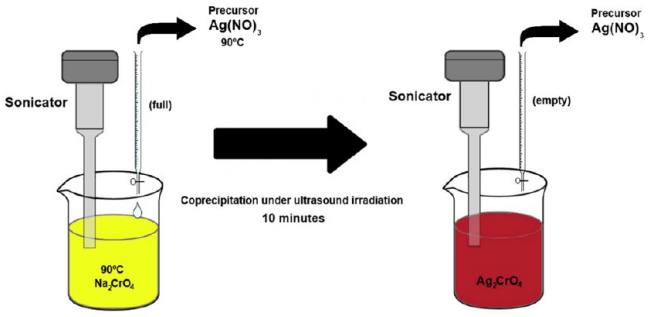

Figure 1. Schematic representation of the synthetic procedure used to obtain Ag_2CrO_4 by the addition of silver nitrate into sodium chromate dropwise in the presence of sonication.

conditions it was possible to observe the formation of a precipitate. The resulting solutions remained under constant magnetic stirring and a temperature of about 90 °C for 30 min. Later, they were washed several times with water and ethanol at 7500 rpm for 5 min. Finally, the dark precipitate was dried in a stove at 60 °C for 24 h.

Therefore, the rapid and homogeneous mixing of the two solutions involved in the coprecipitation process leads to an instantaneous interaction of chromium and silver clusters. The chromium clusters act as network formers (covalent strong bond with oxygen), and most ionic silver clusters are network modifiers. The coprecipitation processes are usually controlled by a growth mechanism-induced Ostwald ripening process, resulting in well-defined morphologies, with a low amount of aggregated particles. On the other hand, a drip process makes it possible to decrease the random nature, involving various interactions times, as well as producing nanoparticles of different sizes and facilitating the formation of aggregates which changes the final morphology. The presence of vibrational energy in the drip process facilitates the organization of the clusters in their rotational movement and decreases the interactions of particles providing greater morphological structure.

The samples were structurally characterized by XRD using a DMax/2500 PC diffractometer (Rigaku) with Cu Kα radiation (λ = 1.5406 Å). The data were recorded in the normal routine for 2θ values ranging from 10° to 75° with a scanning velocity of 2°/min and in the Rietveld routine from 10° to 110° with a scanning velocity of 1°/min, both with a step of 0.02°. Micro-Raman measurements were recorded using a Modular Raman Spectrometer (Horiba, Jobin Yvon), model RMS-550 with Ar laser excitation at 514 nm, and a fiber-microscope operating at 30−1000 cm^{-1}. The shapes, sizes, and elemental distributions of the Ag_2CrO_4 microcrystals were observed with field-emission scanning microscope FE-SEM Inspect F50 model (FEI Company, Hillsboro, OR) operated at 5 kV. UV−vis spectra were recorded using a Varian spectrophotometer (model Cary 5G) in the diffuse reflection mode. PL spectra were collected with a Thermal Jarrel Ash Monospec monochromator and a Hamamatsu R446 Photomultiplier. The 350.7 nm (2.57 eV) exciting wavelength of a krypton-ion laser (Coherent Innova) was used with a laser output of 200 mW. All measurements were carried out at room temperature.

3. THEORETICAL PROCEDURES AND COMPUTATIONAL METHODS

First-principles total-energy calculations were performed using the DFT framework as implemented in the VASP program.[40,41] The generalized gradient approximation in the Perdew−Burke−Ernzerhof formulation for electron exchange and correlation contributions to the total energy was used to solve the Kohn−Sham equations.[42,43] The relaxed systems were generated by means of the conjugated gradient energy minimization scheme when the Hellmann−Feynman forces converged to less than 0.01 eV/Å per atom. Projector augmented wave pseudopotentials were used to describe the electron−ion interaction.[44,45] The plane-wave expansion was truncated at a cutoff energy of 460 eV, and the Brillouin zones were sampled through 6 × 6 × 6 Monkhorst−Pack special k-point grids to ensure geometric and energetic convergence of Ag_2CrO_4 structures. Vibrational frequency calculations were performed at the Γ point, and the dynamical matrix was computed by numerical evaluation of the first derivative of the analytical atomic gradients.

In order to confirm the convergence of the total energy with respect to the slab thickness of different surface models, the surface energy values (E_{surf}) for several low-index planes were calculated using a 6 × 6 × 1 Monkhorst−Pack special k-points grid. E_{surf} was defined as the total energy per repeating cell of the slab (E_{slab}) minus the total energy of the perfect crystal per molecular unit (E_{bulk}) multiplied by the number of molecular units of the surface (n), divided by the surface area per repeating cell on the two sides of the slab as follows: $(E_{slab} - nE_{bulk})/2A$.

The equilibrium shape of a crystal is calculated by the classic Wulff construction, which minimizes the total surface energy at a fixed volume and provides a simple relationship between the surface energy E_{surf} of the (hkl) plane and its distance r_{hkl} in the normal direction from the center of the crystallite. The equilibrium model of the morphology is derived from the calculated surface energies[46−48] verifying the assumption that the crystal faces with the lowest surface energies control the crystal morphology and that the stabilization of the surfaces is based on the atomic configuration of the exposed facets.[49] In this context, first-principle calculations were gradually developed and employed for the study of the crystal morphology. We presented a model based on the Wulff construction, which could explicitly predict the morphology evolution in different

DOI: 10.1021/acs.inorgchem.6b01452
Inorg. Chem. 2016, 55, 8961−8970

environments,[20,24] providing some insights into the features of single-crystal facets that are relevant to subsequent technological applications.

4. RESULTS AND DISCUSSION

4.1. Raman Spectra. Figure 2 shows the experimental Raman spectra for the three samples (1, 2, and 3) of Ag_2CrO_4

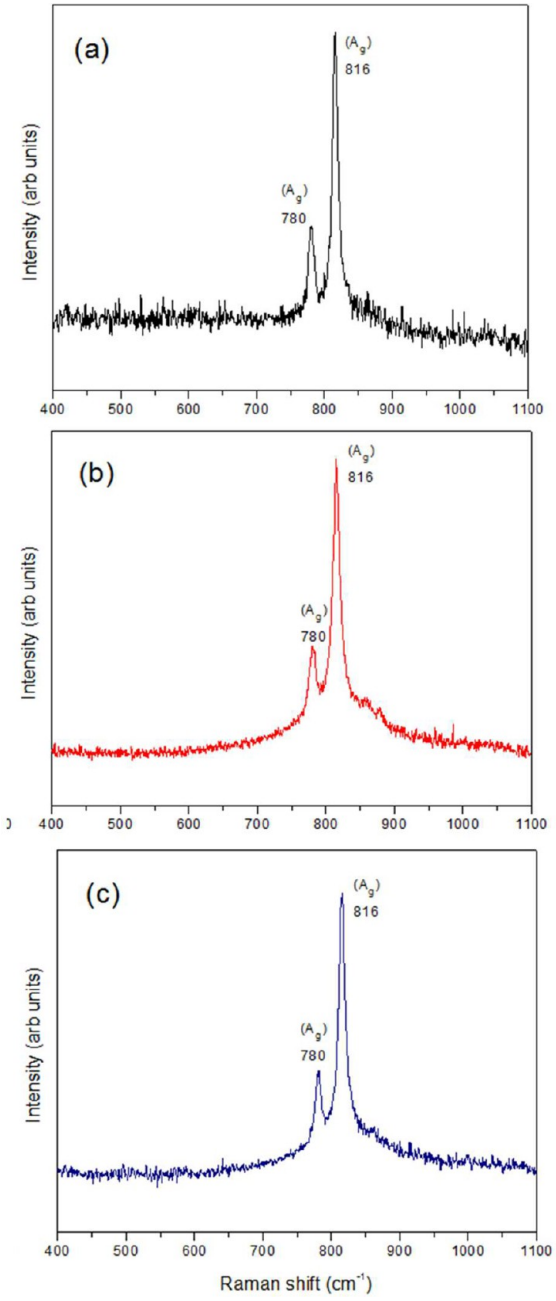

Figure 2. Raman scattering spectra of Ag_2CrO_4 in (a) sample 1, (b) sample 2, and (c) sample 3.

microcrystals. All samples exhibit two strong peaks in the high-frequency region at 780 and 816 cm^{-1}, which are associated with the symmetric stretching vibrations of Cr−O bond in $[CrO_4]$ clusters, ascribed to the A_g mode. Despite the different preparation conditions, the structural order−disorder at short range among the samples presented no huge difference since the active Raman modes were observed in the same frequency region. However, the peaks are relatively wide, indicating some structural disorder at short range.[9]

4.2. FE-SEM Analysis. FE-SEM imaging was carried out in order to study the effect of the preparation conditions. Figure 3 shows the FE-SEM images of all three samples on the same scale (5 μm) to exhibit the difference in the sizes and facets of Ag_2CrO_4 microcrystals. The results indicated that only the

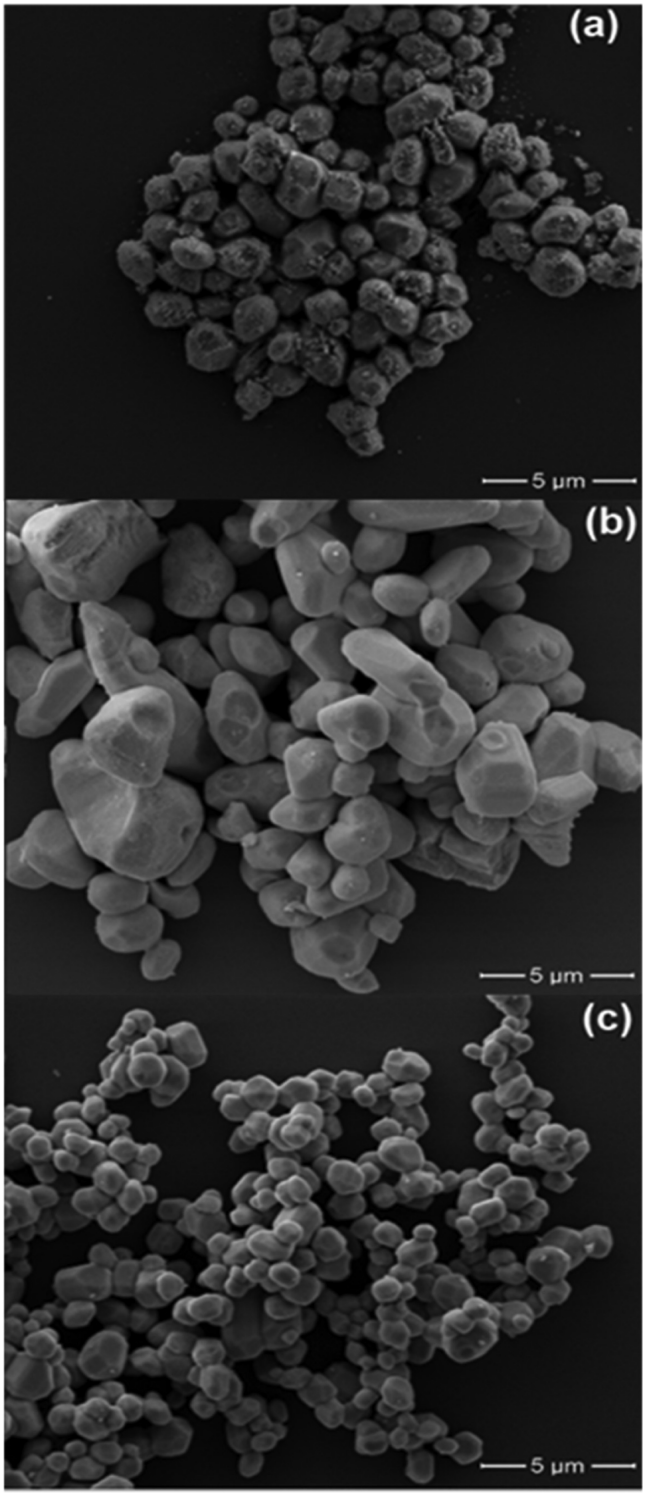

Figure 3. FE-SEM images of Ag_2CrO_4 microcrystals in (a) sample 1, (b) sample 2, and (c) sample 3.

DOI: 10.1021/acs.inorgchem.6b01452
Inorg. Chem. 2016, 55, 8961−8970

change in the condition of Ag precursor addition into chromate precursor is capable of changing the morphology.

During the synthesis along the coprecipitation process when the Ag precursor mixes with different concentrations of CrO_4^{2-} solution, three states can be found: initial, middle, and final stages. Along the initial stage, there is a high concentration of CrO_4^{2-} in the solution that leads to a higher possibility of quick Ag_2CrO_4 formation. In the middle stage, the CrO_4^{2-} concentration is lower than in the initial stage and the formation of Ag_2CrO_4 is more isolated. In the final stage, the low CrO_4^{2-} concentration causes a decrease in the formation of Ag_2CrO_4. As soon as the concentration of CrO_4^{2-} decreases, the effective shocks between the particles also decrease, leading to the formation of smaller particles through the stages.

For sample 1 (Figure 3a), the Ag precursor is added to the chromate precursor at high velocity and the co-precipitation process takes place in a completely random way, generating agglomerates that are less defined and disordered. In this case, the particles do not get enough time to grow because of the fast contact between CrO_4^{2-} and the Ag precursor (high addition rate), leading to the formation of small particles with undefined morphology.

For sample 2, in which the addition rate is lower, the co-precipitation process still occurs in a random way (less random than sample 1). However, because of the lower addition rate, the particles have enough time to grow into small, medium, and large particles and to form agglomerates when the drip meets the chromate solution. Due to the more time available, the particles presented a bigger size.

In sample 3 (Figure 3c), the addition rate was equal to sample 2. The difference between the samples can be seen by comparing Figure 3b and 3c. An analysis of the results renders that in sample 3 smaller particles appear for the same addition rate. This difference is related to the presence of ultrasound irradiation. The ultrasonic waves lead to the formation of lower particles and well-defined facets in the microcrystals. This occurs because the ultrasonic waves decrease the contact between the particles and breaks the possible formation of agglomerates, allowing the particles to organize themselves without the presence of others. In other words, the formation of agglomerates is partially neutralized by the ultrasonic waves. In this case, the time for the particle to grow is the same as sample 2, but the ultrasonic waves hinder the growth process. Therefore, the particles are smaller and less aggregated. The presence of sonication was therefore responsible for the formation of the faceted particles (more defined morphology) when compared to the other preparation conditions. Basically, ultrasound irradiation is related to the formation of well-organized morphologies.

4.3. XRD Analysis. XRD patterns of Ag_2CrO_4 are illustrated in Figure 4. All XRD peaks have sharp and well-defined shapes, which indicates structural order and crystallinity at long range for all samples. The material presents an orthorhombic structure with the space group *Pnma* in agreement with the Inorganic Crystal Structure Database card no. 16298.[50] No deleterious phases were observed in the XRD data.

The average crystallite diameter (D_{crys}) of the powders was determined using the (220), (031), (211), and (002) diffraction peaks of each sample according to the Scherrer equation (eq 1)[51]

$$B = k \times \lambda / D_{crys} \times \cos\theta \quad (1)$$

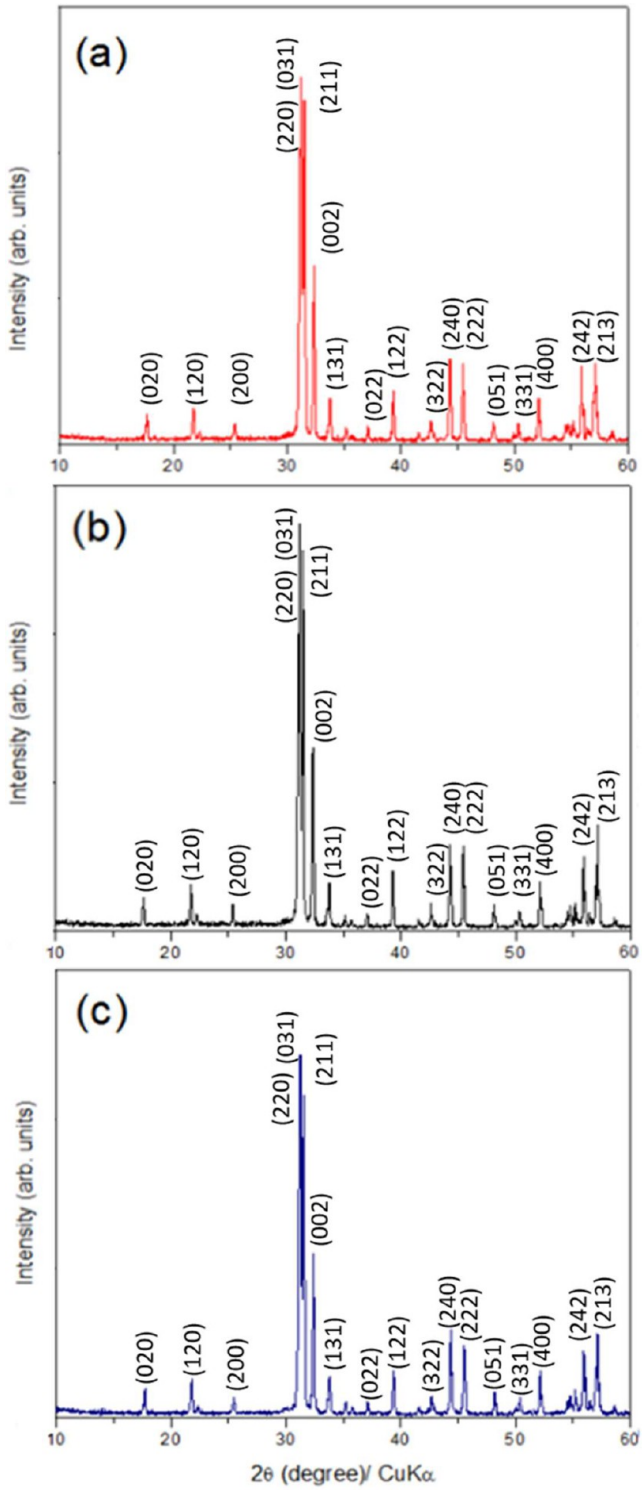

Figure 4. XRD patterns of Ag_2CrO_4 synthesized by the coprecipitation method in (a) sample 1, (b) sample 2, and (c) sample 3.

where B is the full width at half-maximum (fwhm), θ the Bragg angle, k a constant, and λ the wavelength of the Cu Kα radiation. The average crystallite sizes for sample 1, sample 2, and sample 3 are 75.88(37), 98.74(77), and 78.81(26) nm, respectively. More information is collected in Table S1 of the Supporting Information.

The Ag_2CrO_4 structure can be described by the constituent clusters, elongated [AgO_6] octahedra and distorted off-centered

DOI: 10.1021/acs.inorgchem.6b01452
Inorg. Chem. 2016, 55, 8961−8970

$[AgO_4]$ and $[CrO_4]$ tetrahedra, as the building blocks. The orthorhombic unit cell (*Pnma*) of Ag_2CrO_4 contains four formula units occupying Cr atoms at the tetrahedral sites belonging to $[CrO_4]$ clusters, while Ag atoms are located at the tetrahedral and octahedral sites which belong to $[AgO_4]$ and $[AgO_6]$ clusters, respectively, as depicted in Figure 5. The optimized cell parameters are a = 10.176 Å, b = 7.011 Å, and c = 5.618 Å, which are in agreement with the experimental values shown in Table 1.

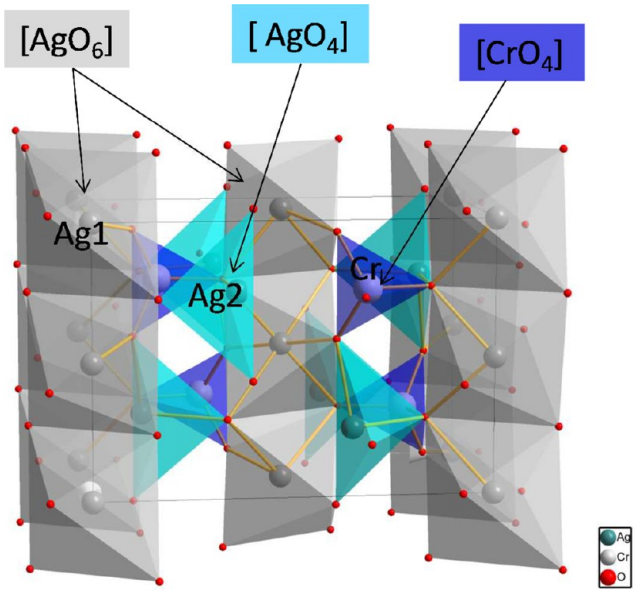

Figure 5. Schematic representation of the cubic structure of Ag_2CrO_4 showing $[AgO_4]$, $[AgO_6]$, and $[CrO_4]$ clusters.

4.4. Theoretical Results. The (001), (010), (100), (011), (110), (101), and (111) surfaces of Ag_2CrO_4 were modeled by an unreconstructed slab model using a optimized equilibrium geometry. To avoid any interaction between surfaces, a vacuum spacer of 15 Å was introduced in the z direction. Slab models (Figure 6) containing 8, 8, 4, 10, 6, 8, and 10 molecular units were considered for the (001), (010), (100), (011), (110), (101), and (111) surfaces, respectively, after some convergence tests of the system. The respective areas were 71.3, 57.2, 39.4, 91.4, 69.4, 81.5, and 99.5 $Å^2$. It is worth noting that all studied surfaces are O and Ag terminated, while the (101) surface is O and Cr terminated. In addition to the atomic configuration of the exposed facets, the coordination environment has a great effect on the reactivity and stabilization of the surfaces. The coordination and distance of the Ag atom, which is more superficial to the closer O atoms, are shown in Figure 6. It is worth noting that surfaces with exposed atoms which are incompletely coordinated usually have a higher reactivity in photocatalytic processes than surfaces with fully coordinated atoms.[18,52,53]

The order of stability of the surfaces is as follows: (001) < (011) < (110) < (010) < (111) and (100). These results can be explained in terms of local order (at short distance) taking into account the vacancies of the O atoms in the superficial Ag ($[AgO_4]$ and $[AgO_6]$) and Cr ($[CrO_4]$) clusters and their symmetry. In some cases, the disorder can be at a medium distance (see Table 2).

Wulff's crystal representation of the optimized Ag_2CrO_4 is depicted in the central part of Figure 7, and the different morphologies can be obtained assuming different values for the surface energies of the different facets. Transformations between the different morphologies are associated with the relative surface energy value of each surface. This interpretation has the advantage that all faces grow from the initial Ag_2CrO_4 crystal (ideal) depending on their surface energy value. Figure 7 illustrates the good agreement between the experimental and the theoretical morphologies. In addition, the original FE-SEM images of Ag_2CrO_4 microcrystals are presented in Figure S1 of the Supporting Information.

The DFT calculations are employed to understand the mechanism of morphological transformation of micro- and nanoparticles at the atomic level. It can also help in choosing the experimental conditions (such as solvent or surfactants) in order to endorse selective interaction to acquire morphological control.

4.5. UV–vis Absorption Spectroscopy. The E_{gap} value can be obtained by the Kubelka and Munk method[54] using eq 2

$$\alpha h\nu = C_1(h\nu - E_{gap})^n \quad (2)$$

where α is the linear absorption coefficient of the material, $h\nu$ is the photon energy, C_1 is a proportionality constant, and n is a constant associated with different kinds of electronic transitions (n = 0.5 for a direct allowed, n = 2 for an indirect allowed, n = 1.5 for a direct forbidden, and n = 3 for an indirect forbidden). According to Xu et al.,[10] the Ag_2CrO_4 crystals exhibited an optical absorption spectrum governed by indirect allowed electronic transitions between the valence and the conduction bands, which leads us to use n = 2 in eq 2. The E_{gap} values obtained for samples 1, 2, and 3 were, respectively, 1.80, 1.70, and 1.78 eV, as shown in Figure 8a. Despite the differences in the preparation conditions of the samples, the optical band gap energy (E_{gap}) of Ag_2CrO_4 obtained experimentally for all samples present no huge difference and is in good agreement with the literature.[9]

The calculated indirect band gap value (Γ–Z) is 1.37 eV, while the direct value of the energy gap is 1.50 eV, slightly lower than the experimentally obtained value. The Brillouin zone with the path used, the band structure, and the DOS projected on atoms are presented in Figure 8b. A general analysis of the DOS shows that the upper part of the valence band consists of noninteracting Ag 4d and O 2p orbitals and a high contribution of Cr 3d and Ag 5s orbitals are observed in the lower part of the conduction band. It should be noted that the calculated band gap is lower than the experimental values

Table 1. Experimental Geometry Data and Rietveld Refinement Parameters for the Three Samples

sample Ag_2CrO_4	a (Å)	b (Å)	c (Å)	V ($Å^3$)	R_{Bragg} (%)	χ^2 (%)	R_{WP} (%)	R_P (%)	S
1	10.065915	7.02457	5.53996	391.72	0.0769	2.349	0.0894	0.0641	1.53
2	10.0667(4)	7.02525	5.54049	391.83	0.0604	2.101	0.0855	0.0583	1.44
3	10.067795	7.02566	5.54123	391.95	0.1060	1.743	0.0930	0.0675	1.32
CIF16298	10.063(11)			391.86					

DOI: 10.1021/acs.inorgchem.6b01452
Inorg. Chem. 2016, 55, 8961–8970

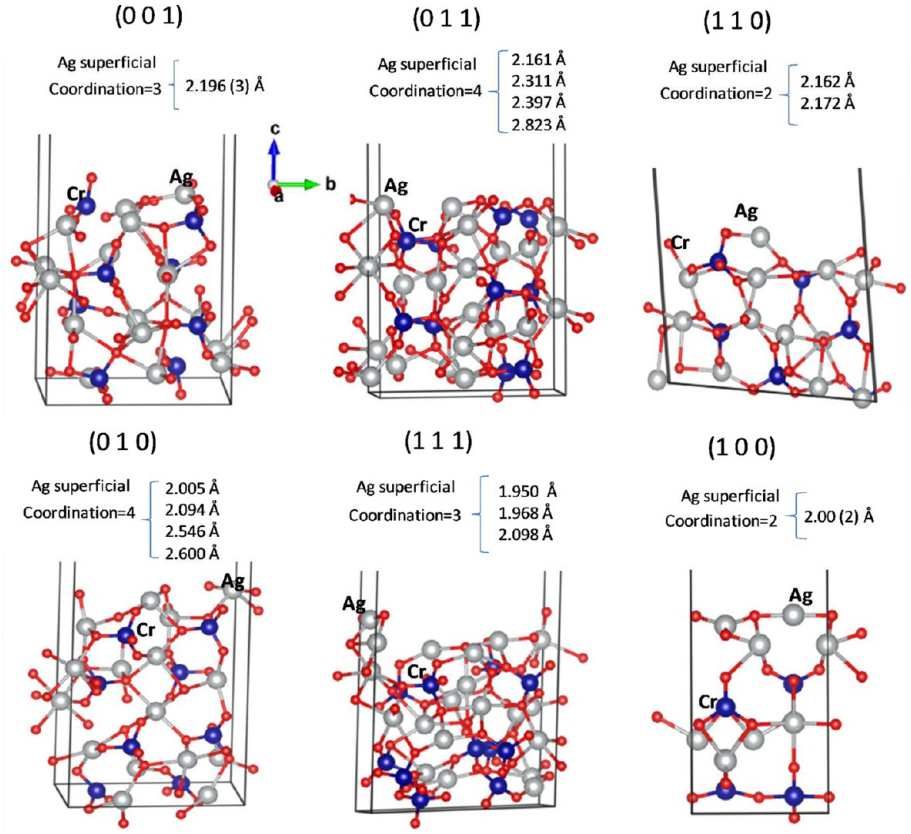

Figure 6. Structure of the (001), (011), (110), (010), (111), and (100) facets based on a slab model. Gray, blue, and red atoms represent Ag, Cr, and O atoms, respectively. The coordination and distance of the Ag atom, which is more superficial to the closer O atoms, are displayed. The number of bonds with equal distances is given in parentheses.

Table 2. Vacancies of O Atoms for the More Superficial Ag ($[AgO_4]$ and $[AgO_6]$) and Cr ($[CrO_4]$) Clusters

surface	O vacancies	disorder
(001)	$[AgO_3{\cdot}3V]_o$ and $[CrO_3{\cdot}V]_d$	short distance
(011)	$[AgO_4{\cdot}2V]_d$ and $[CrO_3{\cdot}V]_d$	short distance
(110)	$[AgO_2{\cdot}2V]_d$ and $[CrO_4]_o$	short distance
(010)	$[AgO_4{\cdot}2V]_d$ and $[CrO_3{\cdot}V]_d$	short/medium distance
(111)	$[AgO_3{\cdot}3V]_d$ and $[CrO_4]_o$	short distance
(100)	$[AgO_2{\cdot}2V]_d$ and $[CrO_4]_o$	short/medium distance

due to the well-known shortcoming of the exchange-correction functional, in agreement with a recently reported work.[55]

4.6. Photoluminescence. Figure 9 shows the PL spectra of Ag_2CrO_4 microcrystals synthesized under sonication. An analysis of the results renders that there is a structural order−disorder at the medium range with two broad bands that can be deconvoluted into six peaks.

PL spectra present a broad band covering the visible electromagnetic spectrum in the range 350−850 nm, and the profile of the emission band is typical of a multiphonon and multilevel process, i.e., a system in which relaxation occurs by several paths involving the participation of numerous states within the band gap of the material.[56,57]

The chemical and physical properties of crystals are determined by the order/disorder of the crystals involving the bulk and clusters at the surface. The clusters and interactions between them are determined by the size of the particles. The interactions between the surfaces and the environment (solvent, precursors, etc.) can be modulated by the temperature, microwave, ultrasonic, pressure, etc. The surfaces are different, not only in the geometry or surface atom electronic density but also in the electronic structure, bonding, and excited states (ability to generate electron−hole pairs (excitons) due to defects), thereby providing different PL efficiencies. Therefore, the formation of different polyhedra results in the variation of the electron density. These effects can result in the production of new levels within the band gap of the semiconductor and improve the charge separations.

From the present results we confirm that the structural defects in the Ag_2CrO_4 microcrystal lattice are responsible for the appearance of intermediate levels between the valence and the conduction bands, which favor the PL emission properties at room temperature. Therefore, these crystals have favorable conditions to promote the process of charge transfer from distorted clusters of the electronic excited states to undistorted clusters located in the ground state. This electronic transition between clusters probably occurs when Ag_2CrO_4 microcrystals with ordered clusters are able to absorb photons. Upon the adsorption of a photon with energy equal to or larger than the band gap of the semiconductor, an electron polaron/hole pair is generated in the bulk/surface and results in the emission of photons with lower energy.

An analysis of the results displayed in Figures 7 and 9 points out that the change in morphology is accompanied by the change in the PL emission. The change in morphology involves different crystallographic surfaces and results in different types of surface electronic structure, featuring different interactions within short (induction interaction) and medium ranges (orientation interaction). The orientation interaction is

DOI: 10.1021/acs.inorgchem.6b01452
Inorg. Chem. 2016, 55, 8961−8970

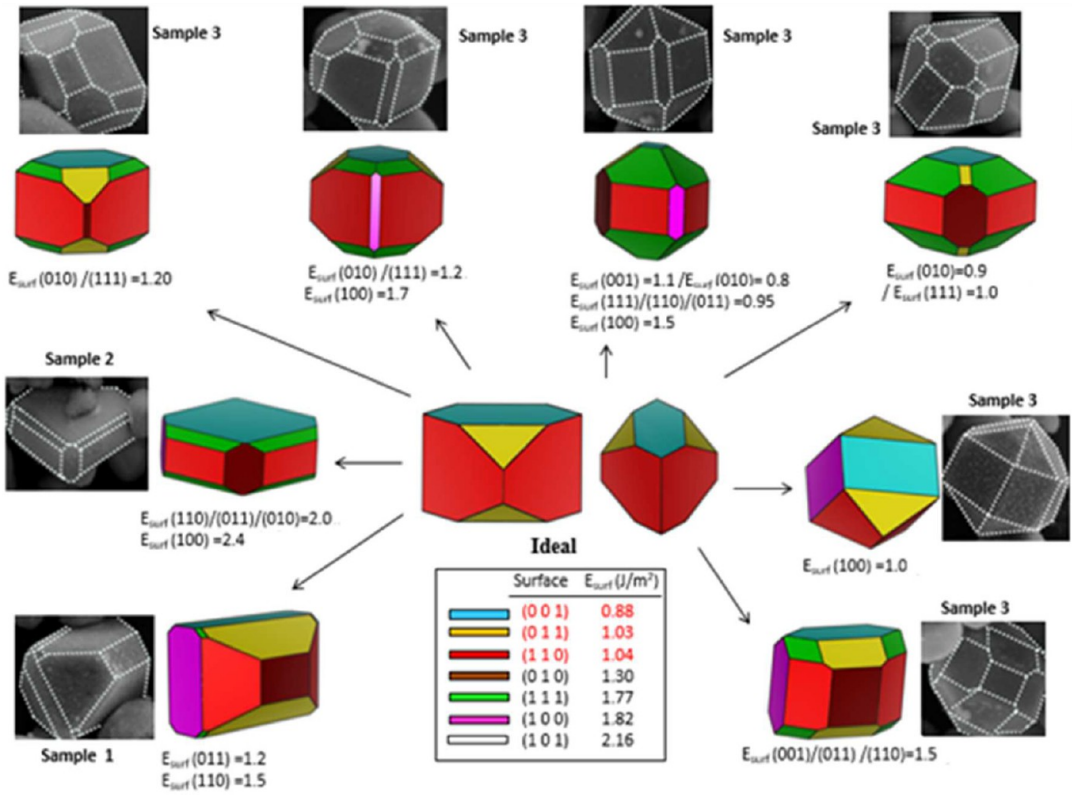

Figure 7. Map of morphologies of Ag_2CrO_4 based on Wulff crystal representations. Surface energy is expressed in Joules per square meter. Experimental FE-SEM images of Ag_2CrO_4 microcrystals of the studied samples are included for comparison.

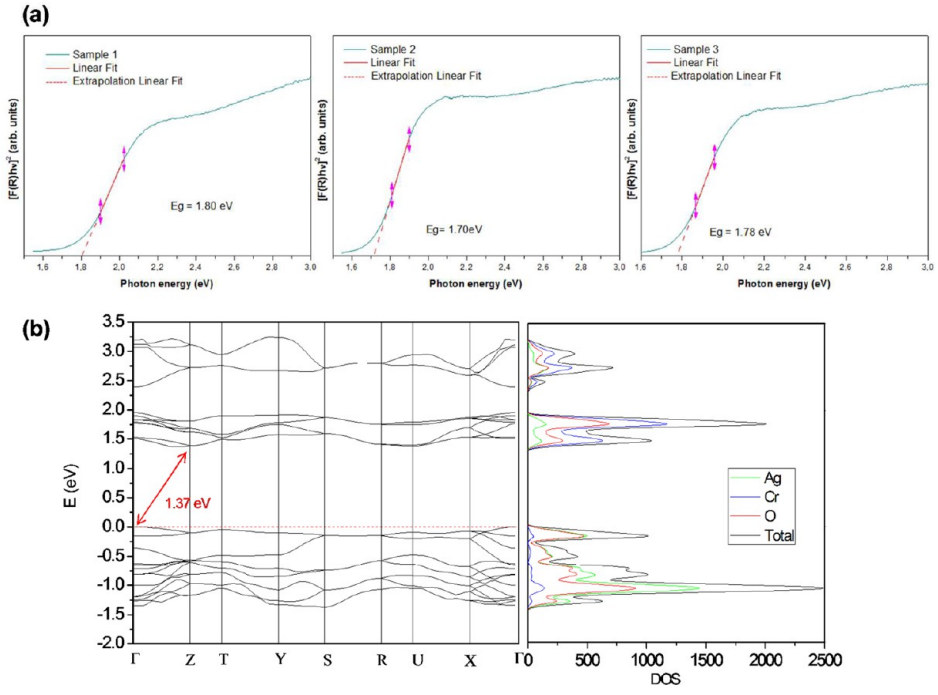

Figure 8. (a) UV−vis spectra of Ag_2CrO_4 samples 1, 2, and 3. (b) Calculated band structure and density of states projected on atoms.

associated with the correlation between the rotational motion of the permanent moments in different complex clusters. Induction interaction occurs via polarization processes of the clusters by the permanent moments of other neighboring clusters. The control of these two types of interactions in the variation synthesis and energy leads to a better control of the semiconductor properties.

Figure 9 shows the PL spectra of Ag_2CrO_4 with broad emission in the blue region (459 nm) and another emission band in the red region (780 nm). It is well known that blue and red emissions arise from the recombination of holes and

DOI: 10.1021/acs.inorgchem.6b01452
Inorg. Chem. 2016, 55, 8961−8970

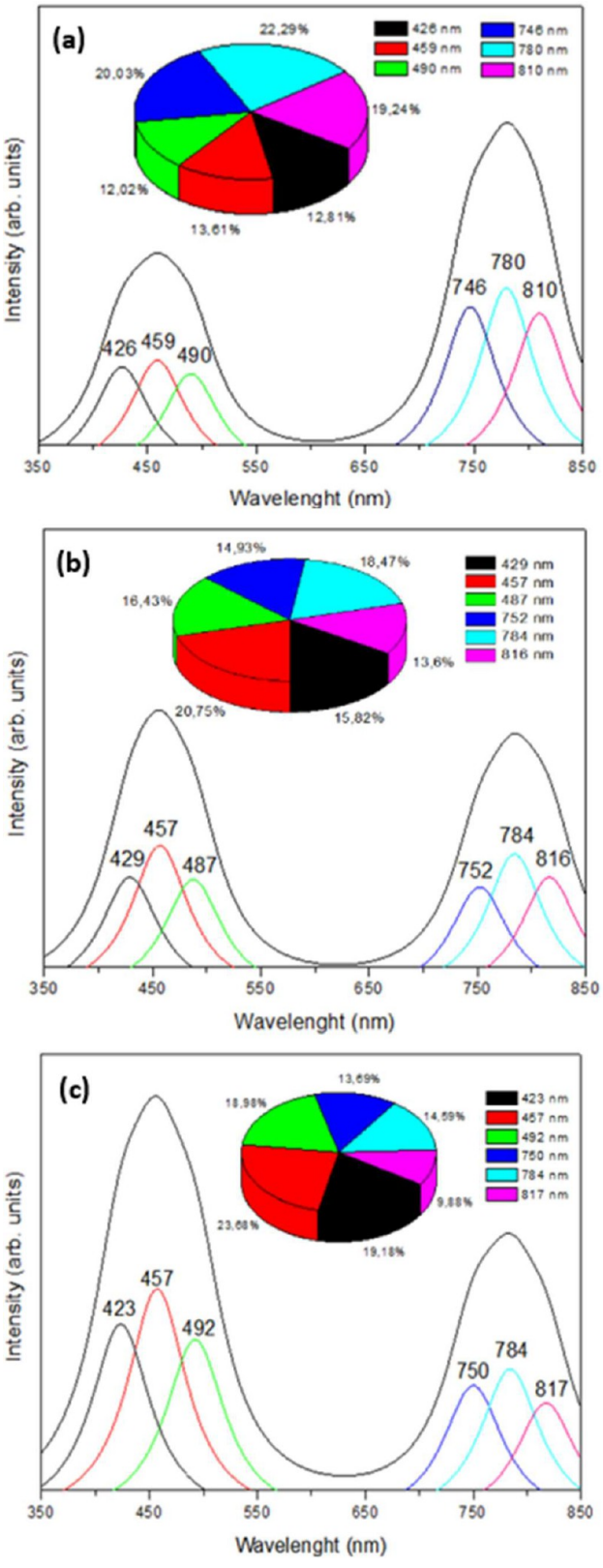

Figure 9. Photoluminescence curve and deconvolution of six peaks of Ag_2CrO_4 microcrystals in (a) sample 1, (b) sample 2, and (c) sample 3.

electrons due to the defects (order−disorder) in the structure of Ag_2CrO_4. The PL spectra show the existence of a binodal curve that characterizes two types of defects in the structure of Ag_2CrO_4. The most energetic band leads to shallow defects, which are associated with the order−disorder clusters, and the other band in the red region is associated with the oxygen vacancy. The coprecipitation method for sample 1 (Figure 9a) produces a structure with more defect density of the oxygen vacancy, while for sample 2 (Figure 9b) a more organized structure is generated. In addition, in sample 3 (Figure 9c) the ultrasonic process produces more shallow defects.

Figure 10 shows the formation of three types of clusters, CrO_4 (Figure 10a), AgO_4 (Figure 10b), and AgO_6 (Figure 10c). Ag ion is more mobile in the clusters AgO_4 and AgO_6 than the Cr ion in CrO_4 cluster, having different coordinations. Accordingly, there is a self-polarization due to the defects generated by the different clusters. Thus, effective charge separation (electron/hole) requires the presence of a cluster-to-cluster transfer process of electrons or holes from $[AgO_4]_o/[AgO_4]_d$ or $[AgO_6]_o/[AgO_6]_d$ or $[CrO_4]_o/[CrO_4]_d$. This order/disorder is dependent upon the morphology of Ag_2CrO_4. The effects of the order−disorder on the $[AgO_4]$, $[AgO_6]$, and $[CrO_4]$ clusters are evidenced when the distances and angles are measured for the three samples. The cluster with more structural disorder among the three samples is $[AgO_4]$, which can also be expressed as $[AgO_{4+2}]$ since there are four distances in the range 2.28−2.43 Å and two distances at 2.94 Å. In addition, the $[AgO_{4+2}]$ cluster has a large variety of angles in the range 64−142°, and this disparity is higher in sample 1. On the other hand, $[AgO_6]$ and $[CrO_4]$ clusters show angles near to 90° and 109°, respectively. These results agree with the PL measurements, which show a variation of shallow and deep defects. According to Figures 7 and 9, there is a higher concentration of deep defects when the reactants are rapidly precipitated. On the other hand, the slow running mixture and vibration provoke the presence of more organized particles, resulting in a higher concentration of shallow defects.

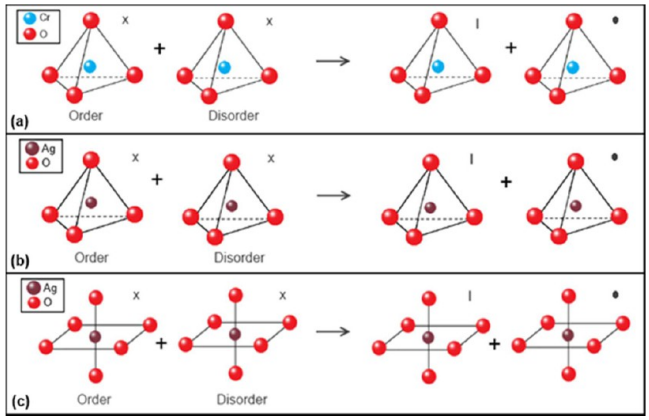

Figure 10. Cluster formation for (a) $[CrO_4]$, (b) $[AgO_4]$, and (c) $[AgO_6]$.

5. CONCLUSIONS

In this work, Ag_2CrO_4 microcrystals were prepared using the coprecipitation method without the use of a surfactant under three different conditions. The XRD patterns of Ag_2CrO_4 present the orthorhombic structure with well-defined diffraction peaks, indicating structural order and crystallinity at long range for all samples, which was confirmed by the Rietveld refinement data. Micro-Raman measurements showed that there were no huge differences between the structural order/

DOI: 10.1021/acs.inorgchem.6b01452
Inorg. Chem. 2016, 55, 8961−8970

disorder at short range. The UV−vis measurements determined the E_{gap} value corresponding to the energy level between the valence band and the conduction band, in agreement with the calculated indirect band gap value of 1.37 eV. The main conclusions of the present work can be summarized as follows: (i) The preparation methods greatly influence the morphology of Ag_2CrO_4 crystals. (ii) Analysis of the corresponding FE-SEM images indicates that as the addition rate of the Ag precursor decreases, the particles have more time to grow and form bigger particles. (iii) When the sonication process is performed, it partially breaks the agglomeration formation, producing smaller and more faceted particles. (iv) DFT calculations can be used to understand the mechanism of morphological transformation of micro- and nanoparticles at the atomic level taking into account that the coordination environment of the exposed atoms in the surfaces has a great effect on its reactivity and stabilization. (v) A relationship among the structural order/disorder effects, morphology, and photoluminescence of the Ag_2CrO_4 microcrystals is found.

■ ASSOCIATED CONTENT

Supporting Information

The Supporting Information is available free of charge on the ACS Publications website at DOI: 10.1021/acs.inorgchem.6b01452.

Crystallite size of products calculated by Debye−Scherrer equation and map of morphologies of Ag_2CrO_4 based on Wulff crystal representations (PDF)

■ AUTHOR INFORMATION

Corresponding Author

*E-mail: lgracia@qfa.uji.es.

Notes

The authors declare no competing financial interest.

■ ACKNOWLEDGMENTS

This work was financially supported by Brazilian research financing institutions (CNPq (304531/2013-8; 237944/2012-0), FAPESP (2013/07296-2; 2013/26671-9), and CAPES (PNPD-1268069)), Spanish research funding institutions (CTQ2012-36253-C03-02 project (Ministerio de Economia y Competitividad)), PrometeoII/2014/022, ACOMP/2014/270 projects (Generalitat Valenciana), and Programa de Cooperación Científica con Iberoamerica (Brasil) of Ministerio de Educación (PHBP14-00020). We also acknowledge Servei Informática, Universitat Jaume I, for the generous allotment of computer time. J.A. acknowledges the Ministerio de Economia y Competitividad, "Salvador Madariaga" program, PRX15/00261. L.G. acknowledges Banco Santander (Becas Iberoamérica: Jóvenes profesores e investigadores).

■ REFERENCES

(1) Xu, D.; Cheng, B.; Zhang, J.; Wang, W.; Yu, J.; Ho, W. *J. Mater. Chem. A* **2015**, *3*, 20153−20166.
(2) Liu, Y.; Yu, H.; Cai, M.; Sun, J. *Catal. Commun.* **2012**, *26*, 63−67.
(3) Cignini, P.; Icovi, M.; Panero, S.; Pistoia, G. *J. Power Sources* **1978**, *3*, 347−357.
(4) Messina, R.; Perichon, J.; Broussely, M. *J. Electroanal. Chem. Interfacial Electrochem.* **1982**, *133*, 115−123.
(5) Ouyang, S.; Li, Z.; Ouyang, Z.; Yu, T.; Ye, J.; Zou, Z. *J. Phys. Chem. C* **2008**, *112*, 3134−3141.
(6) Soofivand, F.; Mohandes, F.; Salavati-Niasari, M. *Mater. Res. Bull.* **2013**, *48*, 2084−2094.
(7) Xu, D.; Cheng, B.; Cao, S.; Yu, J. *Appl. Catal., B* **2015**, *164*, 380−388.
(8) Xu, D.; Cao, S.; Zhang, J.; Cheng, B.; Yu, J. *Beilstein J. Nanotechnol.* **2014**, *5*, 658−666.
(9) Fabbro, M. T.; Gracia, L.; Silva, G. S.; Santos, L. P. S.; Andrés, J.; Cordoncillo, E.; Longo, E. *J. Solid State Chem.* **2016**, *239*, 220−227.
(10) Soofivand, F.; Mohandes, F.; Salavati-Niasari, M. *Micro Nano Lett.* **2012**, *7*, 283−286.
(11) Cheng, L.; Shao, Q.; Shao, M.; Wei, X.; Wu, Z. *J. Phys. Chem. C* **2009**, *113*, 1764−1768.
(12) Demidova, M. G.; Bulavchenko, A. I.; Alekseev, A. V. *Russ. J. Inorg. Chem.* **2008**, *53*, 1446−1454.
(13) Liu, J.-K.; Luo, C.-X.; Quan, N.-J. *J. Nanopart. Res.* **2008**, *10*, 531−535.
(14) West, A. R. *Solid State Chem. Appl.* **2007**, 6−17.
(15) Mousavi, Z.; Soofivand, F.; Esmaeili-Zare, M.; Salavati-Niasari, M.; Bagheri, S. *Sci. Rep.* **2016**, *6*, 20071.
(16) Kuang, Q.; Wang, X.; Jiang, Z.; Xie, Z.; Zheng, L. *Acc. Chem. Res.* **2014**, *47*, 308−318.
(17) Huang, K.; Yuan, L.; Feng, S. *Inorg. Chem. Front.* **2015**, *2* (11), 965−981.
(18) Bomio, M. R. D.; Tranquilin, R. L.; Motta, F. V.; Paskocimas, C. A.; Nascimento, R. M.; Gracia, L.; Andres, J.; Longo, E. *J. Phys. Chem. C* **2013**, *117*, 21382−21395.
(19) Longo, V. M.; Gracia, L.; Stroppa, D. G.; Cavalcante, L. S.; Orlandi, M.; Ramirez, A. J.; Leite, E. R.; Andrés, J.; Beltrán, A.; Varela, J. A.; Longo, E. *J. Phys. Chem. C* **2011**, *115*, 20113−20119.
(20) Andrés, J.; Gracia, L.; Ferrer, M. M.; Gouveia, A. F.; Longo, E. *Nanotechnology* **2015**, *26*, 405703.
(21) Roca, R. A.; Sczancoski, J. C.; Nogueira, I. C.; Fabbro, M. T.; Alves, H. C.; Gracia, L.; Santos, L. P. S.; de Sousa, C. P.; Andres, J.; Luz, G. E.; Longo, E.; Cavalcante, L. S. *Catal. Sci. Technol.* **2015**, *5*, 4091−4107.
(22) Botelho, G.; Andres, J.; Gracia, L.; Matos, L. S.; Longo, E. *ChemPlusChem* **2016**, *81*, 202−212.
(23) Fabbro, M. T.; Saliby, C.; Rios, L. R.; La Porta, F. A.; Gracia, L.; Li, M. S.; Andrés, J.; Santos, L. P. S.; Longo, E. *Sci. Technol. Adv. Mater.* **2015**, *16*, 065002.
(24) Ferrer, M. M.; Gouveia, A. F.; Gracia, L.; Longo, E.; Andrés, J. *Modell. Simul. Mater. Sci. Eng.* **2016**, *24*, 25007.
(25) Kianpour, G.; Salavati-Niasari, M.; Emadi, H. *Ultrason. Sonochem.* **2013**, *20*, 418−424.
(26) Shahri, Z.; Sobhani, A.; Salavati-Niasari, M. *Mater. Res. Bull.* **2013**, *48*, 3901−3909.
(27) Ghaed-Amini, M.; Bazarganipour, M.; Salavati-Niasari, M. *J. Mater. Sci.: Mater. Electron.* **2015**, *26*, 7452−7459.
(28) Ayni, S.; Sabet, M.; Salavati-Niasari, M. *J. Cluster Sci.* **2016**, *27*, 315−326.
(29) Kianpour, G.; Soofivand, F.; Badiei, M.; Salavati-Niasari, M.; Hamadanian, M. *J. Mater. Sci.: Mater. Electron.* **2016**, 1−8.
(30) Kudo, A.; Miseki, Y. *Chem. Soc. Rev.* **2009**, *38*, 253−278.
(31) Jacques, S. D. M.; Leynaud, O.; Strusevich, D.; Beale, A. M.; Sankar, G.; Martin, C. M.; Barnes, P. *Angew. Chem., Int. Ed.* **2006**, *45*, 445−448.
(32) Zhang, G.; Yang, S.; Li, Z.; Zhang, L.; Zhou, W.; Zhang, H.; Shen, H.; Wang, Y. *Appl. Surf. Sci.* **2010**, *257*, 302−305.
(33) Bi, J.; Wu, L.; Zhang, Y.; Li, Z.; Li, J.; Fu, X. *Appl. Catal., B* **2009**, *91*, 135−143.
(34) Sczancoski, J. C.; Bomio, M. D. R.; Cavalcante, L. S.; Joya, M. R.; Pizani, P. S.; Varela, J. A.; Longo, E.; Li, M. S.; Andrés, J. A. *J. Phys. Chem. C* **2009**, *113*, 5812−5822.
(35) De Santana, Y. V. B.; Gomes, J. E. C.; Matos, L.; Cruvinel, G. H.; Perrin, A.; Andres, J.; Varela, J. A.; Longo, E. *Nanomater. Nanotechnol.* **2014**, *4*, 1.
(36) Saberyan, K.; Soofivand, F.; Kianpour, G.; Salavati-Niasari, M.; Bagheri, S. *J. Mater. Sci.: Mater. Electron.* **2016**, *27* (4), 3765−3772.
(37) Cavalcante, L. S.; Almeida, M. A. P.; Avansi, W.; Tranquilin, R. L.; Longo, E.; Batista, N. C.; Mastelaro, V. R.; Li, M. S. *Inorg. Chem.* **2012**, *51*, 10675−10687.

DOI: 10.1021/acs.inorgchem.6b01452
Inorg. Chem. 2016, 55, 8961−8970

(38) Roca, R. A.; Lemos, P. S.; Andrés, J.; Longo, E. *Chem. Phys. Lett.* **2016**, *644*, 68−72.
(39) de Oliveira, R. C.; Assis, M.; Teixeira, M. M.; da Silva, M. D. P.; Li, M. S.; Andrés, J.; Gracia, L.; Longo, E. *J. Phys. Chem. C* **2016**, *120*, 12254.
(40) Kresse, G.; Furthmüller, J. *Phys. Rev. B: Condens. Matter Mater. Phys.* **1996**, *54*, 11169−11186.
(41) Kresse, G.; Hafner, J. *Phys. Rev. B: Condens. Matter Mater. Phys.* **1993**, *47*, 558−561.
(42) Perdew, J. P.; Burke, K.; Ernzerhof, M. *Phys. Rev. Lett.* **1996**, *77*, 3865−3868.
(43) Perdew, J. P.; Chevary, J. A.; Vosko, S. H.; Jackson, K. A.; Pederson, M. R.; Singh, D. J.; Fiolhais, C. *Phys. Rev. B: Condens. Matter Mater. Phys.* **1992**, *46*, 6671−6687.
(44) Blöchl, P. E. *Phys. Rev. B: Condens. Matter Mater. Phys.* **1994**, *50*, 17953−17979.
(45) Kresse, G.; Joubert, D. *Phys. Rev. B: Condens. Matter Mater. Phys.* **1999**, *59*, 1758−1775.
(46) Herring, C. *Phys. Rev.* **1951**, *82*, 87−93.
(47) Wulff, G. Z. *Kristallogr. Miner.* **1901**, *34*, 449−530.
(48) Gibbs, J. W. *Trans. Conn. Acad. Arts Sci.* **1874−1878**, *3* (108−248), 343−524.
(49) Marks, L. D. *J. Cryst. Growth* **1983**, *61*, 556−566.
(50) Hackert, M. L.; Jacobson, R. A. *J. Solid State Chem.* **1971**, *3*, 364−368.
(51) Patterson, A. L. *Phys. Rev.* **1939**, *56*, 978−982.
(52) Bi, Y.; Ouyang, S.; Umezawa, N.; Cao, J.; Ye, J. *J. Am. Chem. Soc.* **2011**, *133*, 6490−6492.
(53) Lazzeri, M.; Vittadini, A.; Selloni, A. *Phys. Rev. B: Condens. Matter Mater. Phys.* **2001**, *63*, 155409.
(54) Kubelka, P. *Zeit Technol. Phys.* **1931**, *12*, 593−603.
(55) Zhang, J.; Yu, W.; Liu, J.; Liu, B. *Appl. Surf. Sci.* **2015**, *358*, 457−462.
(56) Abreu, M. F. C.; Motta, F. V.; Lima, R. C.; Li, M. S.; Longo, E.; Marques, A. P. de A. *Ceram. Int.* **2014**, *40*, 6719−6729.
(57) Nogueira, I. C.; Cavalcante, L. S.; Pereira, P. F. S.; de Jesus, M. M.; Rivas Mercury, J. M.; Batista, N. C.; Li, M. S.; Longo, E. *J. Appl. Crystallogr.* **2013**, *46*, 1434−1446.

DOI: 10.1021/acs.inorgchem.6b01452
Inorg. Chem. 2016, 55, 8961−8970